




Coupling between the photoactivity and CO₂ adsorption on rapidly thermal hydrogenated vs. conventionally annealed copper oxides deposited on TiO₂ nanotubes

Wiktoria Lipińska^{1,*}, Katarzyna Grochowska¹, Jacek Ryl², Jakub Karczewski², Mirosław Sawczak¹, Emerson Coy³, Vincent Mauritz⁴, Ryan W. Crisp⁴, and Katarzyna Siuzdak¹

¹ Centre for Plasma and Laser Engineering, Institute of Fluid–Flow Machinery, Polish Academy of Sciences, Fiszerka 14 Street, 80-231 Gdansk, Poland

² Faculty of Applied Physics and Mathematics, Institute of Nanotechnology and Materials Engineering, Gdansk University of Technology, Narutowicza 11/12 Street, 80-233 Gdansk, Poland

³ NanoBioMedical Centre, Adam Mickiewicz University, Wszechnicy Piastowskiej 3 Street, 61-614 Poznan, Poland

⁴ Chemistry of Thin Film Materials, Department of Chemistry and Pharmacy, Friedrich-Alexander-Universität Erlangen-Nürnberg, Cauerstrasse 3, 91058 Erlangen, Germany

Received: 19 September 2023

Accepted: 11 September 2024

© The Author(s), 2024

ABSTRACT

Highly ordered spaced titanium dioxide nanotubes were fabricated via electrochemical anodization and modified with titania nanoparticles and copper oxides. Such materials were rapidly annealed in hydrogen atmosphere or conventionally in a tube furnace in air, in which the temperature slowly increases. Applied synthesis procedure can be considered as simple, cost-effective, and environmentally friendly as it allows for reduction in used materials and enhances sustainable engineering. Manipulating the chemical composition of materials by different thermal treatments resulted in various photoelectrochemical activities and density of CO₂ adsorption sites. Rapidly annealed nanotubes decorated by copper oxides exhibit excellent electrochemical properties where one electrode combines both: solar to electricity conversion (photocurrent under visible light 30 μA/cm²) and CO₂ adsorption systems (18 times higher current after CO₂ saturation). Rapidly thermal hydrogenated TiO₂ nanotubes with copper oxides had 17 times higher photocurrent and wider absorption band (380–780 nm) than conventionally annealed ones. Furthermore, the crystal planes such as Cu (111), Cu (220), Cu₂O (110), CuO (002) and Cu⁰, Cu⁺, Cu²⁺ oxidation states, and oxygen vacancies were recognized for hydrogenated sample. It should be highlighted that thermal annealing conditions significantly affects ability of copper oxide to CO₂ adsorption and CO₂ reduction reaction for hydrogenated electrode.

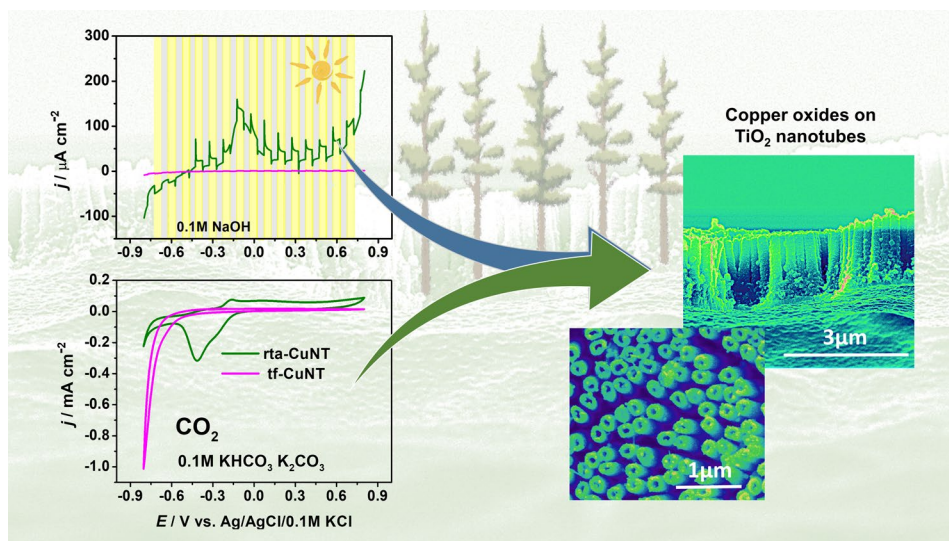
Handling Editor: N. Ravishankar.

Address correspondence to E-mail: wlipinska@imp.gda.pl

<https://doi.org/10.1007/s10853-024-10223-4>

Published online: 19 September 2024

GRAPHICAL ABSTRACT



Introduction

The enhancement of CO_2 concentration in our atmosphere is caused by industrialization and combustion of carbon and oil energy resources. In nature CO_2 is required for photosynthesis which occurs within chloroplasts of plants and mushrooms cells during Calvin cycle. However, our ecosystem is not enough efficient because the rate of CO_2 capture is lower than its release into air [1]. Therefore, many efforts are undertaken to develop the field of renewable energy, namely solar, wind, or biomass, to reduce the amount of emission. Except for replacing fossil fuels with renewable energy sources, also converting CO_2 to chemicals like CO , CH_4 , CH_3OH , $\text{C}_2\text{H}_5\text{OH}$, or HCOOH , is of key importance. Furthermore, another strategy to mitigate the emission of greenhouse gases into the atmosphere is CO_2 capture and separation based on chemical/physical adsorption [2]. Nowadays development of unique functional materials and innovations is crucial to fabricate the renewable energy sources. Minimization of increasing environmental footprint, by usage of cost-effective and environmentally friendly materials, allows for more sustainable development of our planet's resources.

TiO_2 has been one of the most extensively investigated semiconductor from 50 years [3], because of its unique properties, such as high photocatalytic activity, resistance to photocorrosion, chemical stability, good adsorption affinity for organic compounds

(in the anatase form) [4], as well as non-toxicity and availability. Interestingly, it was proven that various geometries of titanium dioxide materials exhibit different photoelectrolysis activities [5] as higher specific surface area results in more surface reactive sites. Among other nanostructures, titania nanotubes are widely applied because of their good accessibility and excellent control of their architecture depending on the applied anodization parameters for adsorption, functionalization, and enhancement of electron transfer properties [6]. It should be highlighted that the fabrication of TiO_2 nanotubes via electrochemical anodization can be easily scalable from laboratory to industrial scale [7]. Moreover, it is a cost-effective process which can be carried out in simple working setup resulting in formation of high-quality, homogeneously distributed and ordered titanium dioxide layer [8]. Furthermore, TiO_2 can serve not only as a standalone material, though its wide energy band gap (ca. 3.2 eV for anatase) limits photoactivity to UV light but also can be used as a stable support to form composites with other compounds or metals such as Au, Ag, Pd, and Cu. Such a strategy can provide completely new material properties exhibiting improved light absorption in the visible region since, for nanometre size metal or metal oxide nanoparticles, the quantum confinement effect significantly alters the properties of the nanomaterial [9, 10].

Recently, much higher interest in utilization of non-noble metals, like copper, is used for this catalytic

purpose. It is recognized as a promising candidate due to the face-centred cubic structure and its electronic configuration, with properties like those of silver and gold. However, its abundance on Earth is much higher than noble metals, thus making copper much cheaper and available. In composites containing copper species, it can take various oxidation states: 0, +1, and +2. Moreover, when TiO_2 is coated with metallic copper under anaerobic conditions both metallic and oxide Cu species are observed. Taking into account the fact that often such electrodes are later stored in aerobic conditions enabling surface oxidation to occur, an accurate description of each Cu species role in the conducted reactions at the electrode surface may be complicated. Apart from the surface modification, changes introduced in the bulk material can be crucial for conductivity improvement. Among other routes, like introduction into the crystal structure foreign metal and non-metal atoms (i.e. dopants), formation of the non-stoichiometric material via hydrogenation is a simple method to increase donor densities. This process is realized mostly via an electrochemical or thermally assisted procedure, but depending on the chosen method, the stability of the obtained product varied [11]. Thermal annealing in a hydrogen atmosphere results in the formation of oxygen vacancies and induces surface disorder [12, 13]. The creation of mid-gap energy levels between the valence and conduction bands is then responsible for enhanced absorption of light [14]. However, this strategy may be insufficient to enhance the photoresponse of the material, and both surface decoration combined with bulk modification should be carried out. Such an approach was realized by Wu et al [15] who decorated hydrogenated TiO_2 nanofibers by various metal nanoparticles including Ag, Cu, Pd, and Pt. The Pd:H: TiO_2 electrode exhibited the highest photoresponse due to the presence of defects such as oxygen vacancies and Ti^{3+} in hydrogenated TiO_2 as well as beneficial light harvesting and improved charge transport because of the presence of metal particles.

In this paper, we take advantage of the combined modification route and apply both hydrogenation and decoration of titania nanotubes with copper species to improve photoactivity and CO_2 adsorption. TiO_2 nanotubes, characterized by the spacing between each tube, were prepared by electrochemical anodization of titanium foil and then immersed in TiCl_4 solution. This strategy leads to roughening of the surface and enhances the overall area of the nanotube. Afterwards,

10 nm-thin Cu layer was sputtered, and rapidly thermal-treated under hydrogen atmosphere or conventionally annealed in a tube furnace. As already mentioned above, the synthesis method of material preparation is cost-effective and can be applied at industrial scale. Proposed fabrication procedure has minimal influence on the environment. Magnetron sputtering of thin copper layer is carried out in closed chamber where metal layer is directly immobilized on nanotubes. Therefore, such materials can be easily utilized and regenerated in contrast to, for example, suspension of nanoparticles. The morphology of prepared electrodes was verified using a scanning electron microscope, while the structural and chemical nature was identified by analysis of X-ray diffraction patterns and X-ray photoelectron spectra, respectively. Optical properties and photoluminescence of prepared materials were also studied, as well as the electrochemical and photoelectrochemical performance. The results obtained show that the proposed fabrication protocol can be applied in the development of nanostructures used in the field of photoelectrochemistry and CO_2 adsorption or transformation.

Experimental

Reagents

Titanium foil (99.7%, thickness: 0.127 mm, Strem), acetone (99.5%, Chempur), ethanol (96%, Chempur), diethylene glycol (99.5% Chempur), hydrofluoric acid (Chempur), ammonium fluoride (98%, Chempur), copper target (99.99%, Quorum Technologies), hydrogen (99.9%, Air Liquide), potassium hydrogen carbonate (98.5%, Chempur), potassium carbonate (99.0%, Chempur). All chemicals used were of analytical purity grade.

Electrode fabrication

The Ti foil was cut into $2 \times 3 \text{ cm}^2$ plates and ultrasonically cleaned in acetone, ethanol, and water for 10 min. Titania nanotubes were fabricated using an anodization process in a two-electrode system, where Ti was an anode and Pt mesh was a cathode. The electrolyte contained 0.09 M NH_4F /1.3% vol HF/6.2% vol H_2O /92.5% vol diethylene glycol. The anodization was carried out at the temperature of 40 °C with the use of thermostat (Julabo F-12) and at the applied

voltage of 40 V for 2 h. The obtained titanium dioxide nanotubes (TN) were then thermally treated in a rapid thermal annealing (RTA) furnace (MILA 5000 P-N) with a rate of 37.5° C/s for 15 min at 450 °C in hydrogen atmosphere (rta-TN) or in conventional tube furnace (Nabertherm) with a rate of 2° C/min for 2 h at 450 °C in air (tf-TN). In the case of copper-modified nanotubes, their surface was developed by an additional porous layer of TiO₂ (TN were not calcined beforehand) after the anodization process enabling an increase of the surface area [16, 17]. In the first step the nanotubes were immersed for 30 s in 0.1 M TiCl₄ solution in water that was stored in ice bath. The electrodes were left for 30 min in 0.1 M TiCl₄ solution on a hot plate at 100 °C. The second stage covers the electrode rising with deionized water. This procedure was repeated three times. For further modification, a 10-nm layer of copper was deposited using magnetron sputtering (Q150T S system, Quorum Technologies). Finally, samples were thermally treated in an RTA (rta-CuTN) or in a tube furnace (tf-CuTN).

Sample characterization

The morphology of electrodes was inspected by a field emission scanning electron microscope (SEM, FEI Quanta FEG250) equipped with a secondary ET detector and with the beam accelerating voltage kept at 10 kV. Selected samples were inspected in high-resolution transmission microscopy (HR-TEM). Their preparation was carried out by scratching the NTs surface over a commercially available Ni-Grids. The samples were then inspected for particulate matter in the microscope. Samples were investigated in a HR-TEM microscope equipped with EDX detector (JEOL ARM-200F).

The optical properties were investigated using a UV–vis spectrophotometer (Lambda 35, Perkin-Elmer) equipped with a diffuse reflectance accessory. Spectra were recorded in the range of 300–800 nm with a scanning speed of 60 nm/min. The fluorescence spectra were recorded by means of a custom-built setup equipped with 365 nm 500 mW UV LED used as an excitation source. In front of the UV LED, a bandpass filter (UG11, Schott) was used to reduce residual LED radiation in the visible range. The layer of nanotubes was excited at an angle of 45 degrees. The fluorescence signal was collected using a quartz lens and focused on the entrance of an optical fibre. Additionally, in the detection path, a bandpass filter (GG400, Schott) was

used for blocking the excitation wavelength. The fluorescence signal was analysed using a 0.3-m monochromator (SR303i, Andor) equipped with 600 groves/mm grating and recorded with an ICCD detector (DH740, Andor).

The crystal structure was verified using an X-ray diffractometer (XRD, Bruker D8 Advance) equipped with Lynxeye XE-T detector with Cu_{Kα} X-Ray generator.

The X-ray photoelectron spectroscopy (XPS) analysis was carried out by an Escalab 250Xi (ThermoFisher Scientific), using an Al_{Kα} X-ray source. The high-resolution spectra were recorded in the core binding energy range of Cu2p, Ti2p, O1s, with 20 eV pass energy through the hemispherical analyser. The supporting Cu_{KLL} Auger peak was recorded. Finally, the peaks were adjusted according to the adventitious carbon C1s (284.6 eV).

Electrochemical and photoelectrochemical properties were measured using an AutoLab PGStat 302N potentiostat–galvanostat. Measurements were taken in 3 electrode arrangements, where prepared samples were used as working electrode, Pt gauze as counter electrode and Ag/AgCl/0.1 M KCl as reference electrode. Cyclic voltammetry (CV) and linear voltammetry (LV) measurements were taken in deaerated 0.1 M NaOH solution in the range from –0.8 V to +0.8 V versus Ag/AgCl/0.1 M KCl. The CVs were performed with a scan rate of 50 mV/s, while the LVs with a scan rate of 10 mV/s. The LV curves were recorded in the dark and under light illumination provided by a xenon lamp (LOT-Quantum Design GmbH). To expose the working electrode to visible light, an optical filter (GG420 Schott) was applied to cut off wavelengths below 420 nm. Therefore, the arrangement of the experimental setup enables electrochemical measurements when the working electrode is exposed to vis or UV–vis irradiation. The light intensity was calibrated by the silicon cell (Rera) and equalled 100 mW/cm².

The 3D map of the photocurrent density was registered by a photoelectric spectrometer (Instytut Foto-nowy) equipped with a 150-W Xe lamp. Measurements were taken in 0.1 M NaOH solution at +0.4 V and +0.5 V versus Ag/AgCl/0.1 M KCl from 300 to 600 nm.

CV measurements were taken on CO₂-saturated 0.1 M KHCO₃ and K₂CO₃ electrolyte (pH = 10) when no NaOH was present. Furthermore, measurements were taken in CO₂-saturated 0.1 M KHCO₃ and K₂CO₃ electrolyte with additional 0.5 M NaOH in

order to increase the pH to 14 measured using a pH metre (ChemLand, MP-103).

Results and discussion

Morphology of prepared electrodes

The anodization process provides ordered, spaced TiO_2 nanotubes (Fig. 1). The diameter of non-modified nanotubes is equal to 192 ± 20 nm and $195 \text{ nm} \pm 20$ nm for the samples rta-TN (Fig. 1c) and tf-TN (Fig. 1g), respectively. The samples after treatment with TiCl_4 and copper species have wider edges of the tubes. As also observed by Meen et al. [17], TiCl_4 treatment makes primarily smooth nanotubes rougher, causing a large increase in the overall surface area of TiO_2 nanotubes. The SEM image of TN modified by TiCl_4 but without Cu is shown in Figure S1. The rta- TiCl_4/TN and tf- TiCl_4/TN nanotubes wall thickness was equal to $80 \text{ nm} \pm 25$ nm and $90 \text{ nm} \pm 24$ nm, respectively. In the case of the rta-CuTN rapidly annealed in hydrogen atmosphere, they are characterized by an outer diameter of $220 \text{ nm} \pm 10$ nm and an inner diameter of $86 \text{ nm} \pm 12$ nm, while for the tf-CuTN treated in the tube oven outer diameter of $250 \text{ nm} \pm 20$ nm and an inner diameter of $37 \text{ nm} \pm 10$ nm. The heights of the rta-CuTN and rta-TN are the same and equal to ca. $1.55 \mu\text{m} \pm 0.05 \mu\text{m}$. In the case of the tf-CuTN and tf-TN annealed in a tube furnace, their height reaches $1.63 \mu\text{m} \pm 0.10 \mu\text{m}$ and $1.67 \mu\text{m} \pm 0.09 \mu\text{m}$.

TEM images were obtained for two types of samples, rta-CuTN (Fig. 2) and tf-CuTN (Fig. 3). The localization of titanium and oxygen are similar but the significant difference in copper distribution is observed. In the case of tf-CuTN, copper is uniformly distributed along the tube walls, while for the rta-CuTN, according to the localization of shiny green region, it occupies topmost area of the tube. It corresponds to the spherical particles visible on the tip of the nanotubes visible in the SEM image given in Fig. 1a. The combined EDX spectra indicating the presence of metallic copper (Fig. 2h). The cork-like shape formation in the nanotubes outlet of rta-CuTN material may affect both the recorded XPS spectra in the binding energy regime for $\text{Cu}2p$ as well as the electrochemical performance.

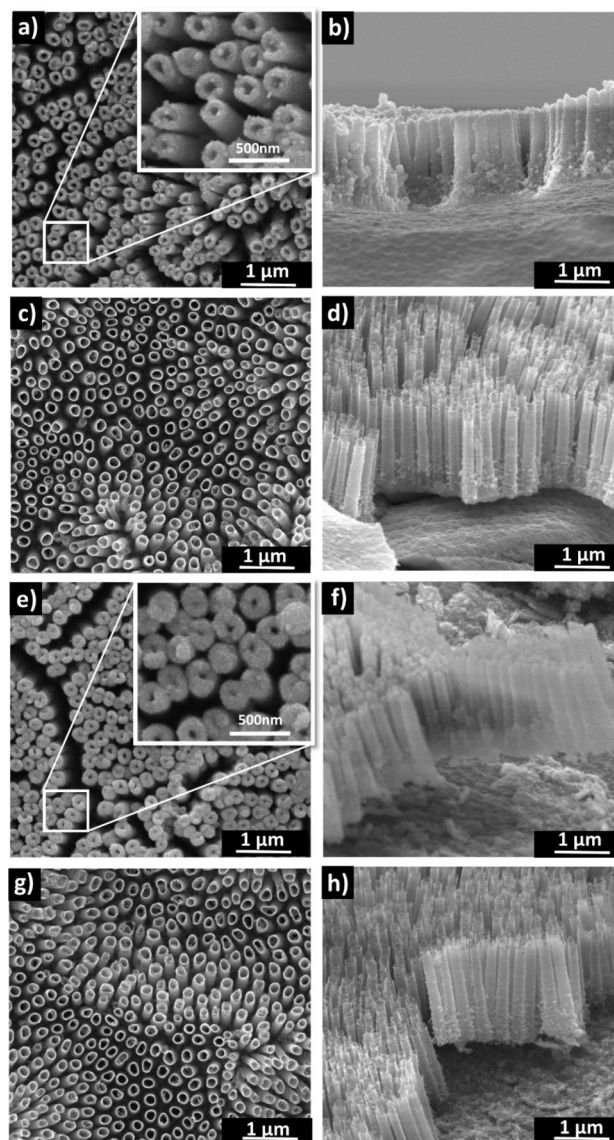


Figure 1 SEM images of **a, b** rta-CuTN, **c, d** rta-TN, **e, f** tf-CuTN, and **g, h** tf-TN.

Optical properties of electrode material

The optical properties of the prepared samples were investigated by means of UV–Vis reflectance spectroscopy. As shown in Fig. 4a, all electrodes exhibit strong absorption in the UV region originating from the titania [18]. The most obvious enhancement in absorption after deposition of Cu on TiO_2 nanotubes annealed in conventional furnace can be seen in the range of 350–500 nm, similar to the work of Molenda et al. [19]. Furthermore, the rta-CuTN electrode has also strong absorption in the visible range: from 380 to

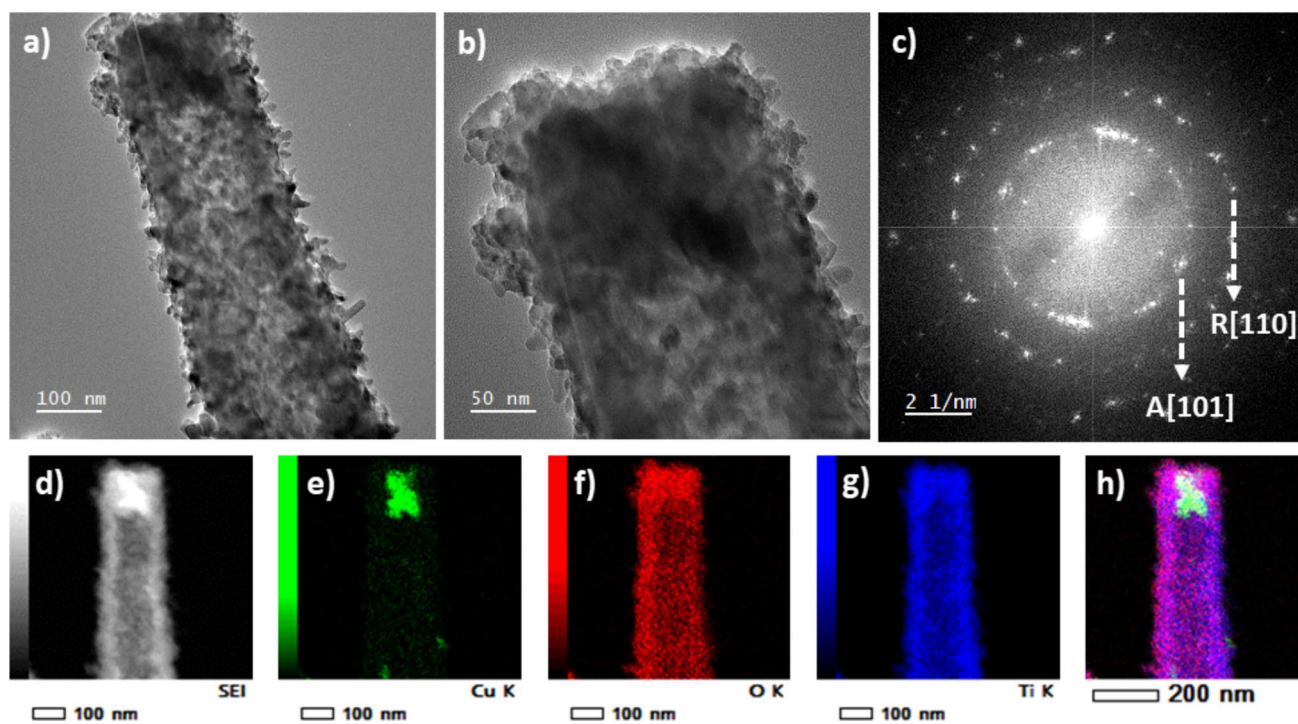


Figure 2 a–c TEM and d–h EDX images for the rta-CuTN.

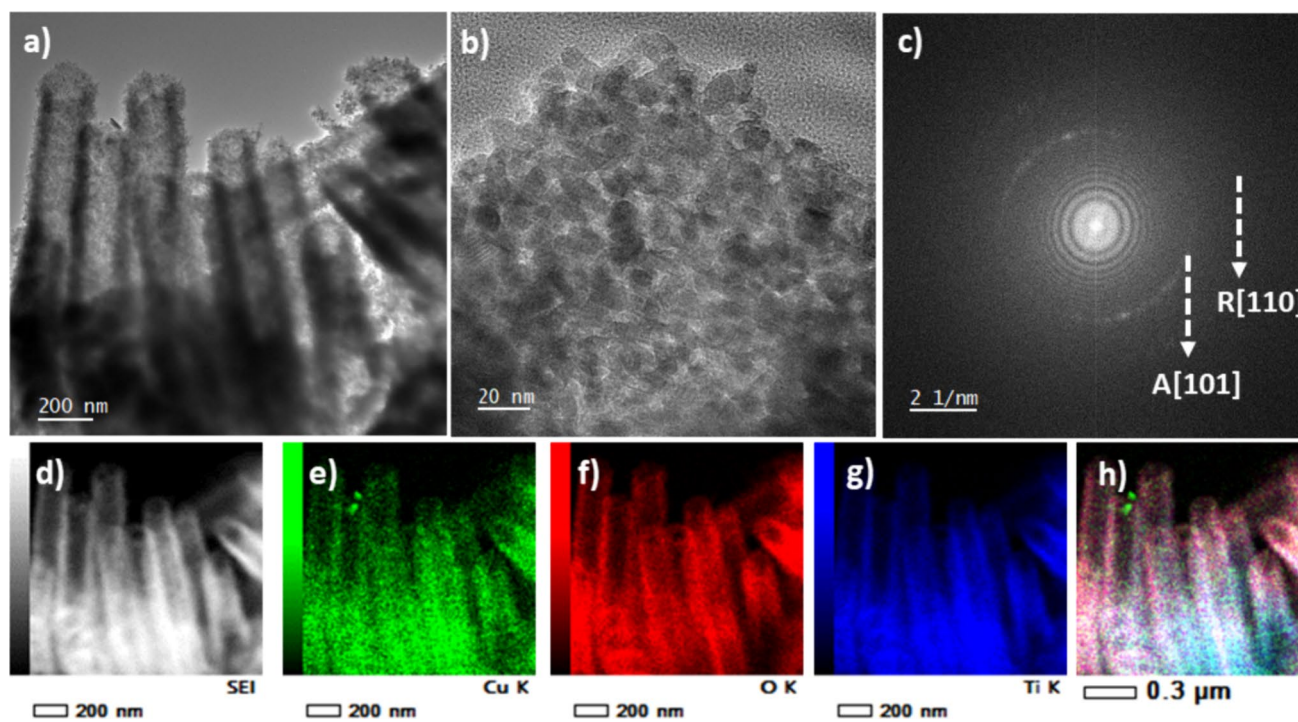


Figure 3 a–c TEM and d–h EDX images for the tf-CuTN.

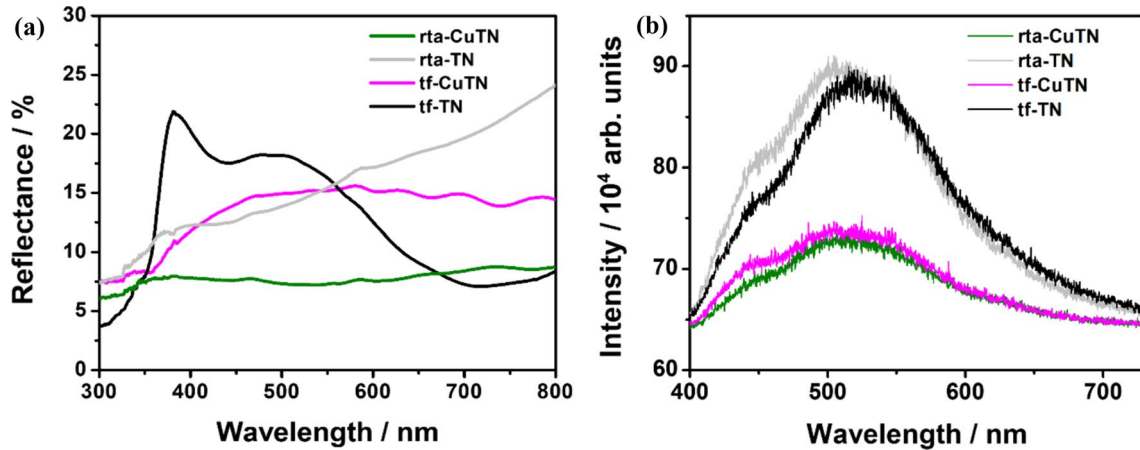


Figure 4 **a** UV–vis reflectance and **b** photoluminescence spectra of pure TN and TN with increased area modified by copper.

780 nm. This can be explained by the presence of the copper species with different oxidation states of Cu, confirmed by the XPS analysis. Moreover, it should be underlined that the presence of oxygen vacancies in rta-CuTN sample treated in hydrogen atmosphere can be also responsible for this feature. According to Gharaei et al. [20] the Cu doping is found to modify the TiO₂ nanotubes by creation of sub-bands and prevention of electron–hole recombination. However, it should be noted that not only the copper but also the additional loading of titania on TiO₂ nanotubes due to treatment in TiCl₄ solution increases the absorbance in the range of 400–800 nm [21] (see Fig. S2). Moreover, the rta-TN differs significantly from the tf-TN in the range of 400–500 nm. Siuzdak et al. [22] discussed the narrowing of the band gap of hydrogenated TiO₂ nanotubes by formation of surface defects, oxygen vacancies, and introduction of additional mid-gap states. The photoluminescence spectra of modified and non-modified electrodes are shown in Fig. 4b. Under excitation by UV light, a wide emission band in the visible range is observed and is associated with exciton recombination and oxygen defects related to shallow (in the case of pure TiO₂) and deep (Cu-modified samples) trap centres [23, 24]. The photoluminescence is lowered in samples incorporating Cu (Fig. 4b). This change is reported by others [24, 25] who explain it by grain boundary defects as non-radiative centres responsible for shallow trap centre formation.

Detailed analysis of the photoluminescence spectra given in Fig. 5 shows that they consist of a series of bands, the position, and relative intensity of which change depending on the sample processing method

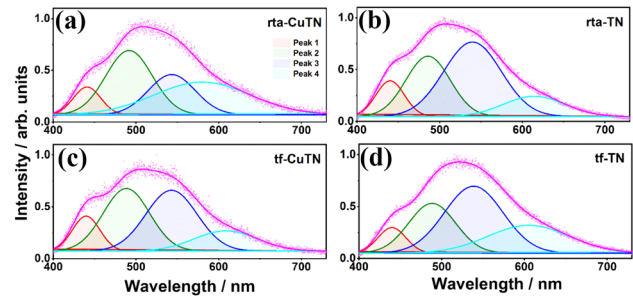


Figure 5 Normalized photoluminescence spectra of **a** rta-CuTN, **b** rta-TN, **c** tf-CuTN, **d** tf-TN.

Table 1 Photoluminescence spectra band peak positions

Sample	Peak 1 (nm)	Peak 2 (nm)	Peak 3 (nm)	Peak 4 (nm)
rta-TN	440.1	485.9	539.7	614.2
tf-TN	439.8	488.4	538.7	605.1
rta-CuTN	440.9	491.6	543.2	579.9
tf-CuTN	439.6	488.3	542.9	608.5

and the presence of Cu. As a result of deconvolution of each emission spectrum, four Gaussian signals centred near 440, 490, 540, and 600 nm can be distinguished. In the literature, one may find the discussion on the origin of the emission in certain spectral ranges on the basis of various dopants. The band located near 440 nm is related to self-trapped excitons [26]. Analysing the results presented in Fig. 5 and in Table 1, the position of this band does not change depending on the method of sample preparation. In the case of the rta-TN and tf-CuTN samples, a slight increase in the intensity of this band is observed. Emission

bands centred near 490 and 540 nm are most probably related to the oxygen vacancies with zero, one, or two trapped electrons resulting from the shallow and deep-level vacancies in the band gap of TiO_2 [24, 27, 28]. It can be observed that the position and relative intensities of these two bands vary depending on the method of sample preparation and the presence of Cu. In the case of Cu-modified samples, the intensity of the band located around 490 nm clearly increases while the intensity of the 540 nm band decreases. According to Lei et al. [23] the band centred near 540 nm is associated with shallow-level oxygen vacancies with one trapped electron while the shorter wavelength emission is associated with vacancies with two trapped electrons.

Crystallinity of prepared samples

The XRD diffraction patterns for the rta-CuTN, rta-TN, tf-CuTN, and tf-TN electrodes are shown in Fig. 6. The reflections located at 25.4° , 36.8° , 37.9° , 38.5° , 48.1° , 54.1° , 55.1° , 59.4° , 63.0° , 67.3° , 76.2° correspond to the following anatase TiO_2 crystal planes: (101), (103), (004), (112), (200), (105), (211), (132), (204), (116), and (301), respectively [28, 29]. It should be highlighted that anatase is dominant oxide phase for all electrodes. Figure S3 shows the magnification of XRD pattern for anatase (101) crystal plane. The shift of the reflection angles can indicate the presence of oxygen vacancies [30]. In the case of the tf-CuTN electrode, no shift in

relation to the tf-TN electrode can be observed. However, for the rta-CuTN and the rta-TN shift relative to the tf-TN might indicate vacancies which was confirmed by XPS analysis. Weak rutile (110) and (111) crystal planes can be recognized at 27.5° and 36.1° [31, 32]. Moreover, reflections located at 35.2° , 40.2° , 53.2° , 70.8° , 77.4° correspond to (100), (101), (102), (110), and (201) Ti planes, respectively, where (101), (102) and (110) are the most intense ones. Signals originating from the Ti are typical when the material is formed on Ti foil via the anodization route. In the case of the rta-CuTN Cu (111) and (220) as well as Cu_2O (110) or CuO (002) crystal planes were recognized to be present at the surface, further confirmed with XPS analysis [33–35]. Rapid thermal annealing of copper oxides in a hydrogen atmosphere results in the formation of different copper crystallographic planes in contrast to conventionally annealed copper. According to Wu et al. [36] annealing of copper in reducing atmosphere leads to growth of high-index copper faces. The most significant anatase planes of (101) and (112) are ca. 2 and 6 times more intense for the tf-CuTN than for the rta-CuTN. Differences in intensity and width can be related to various grain size of TN modified by TiO_2 using TiCl_4 annealed rapidly in RTA or conventionally in tube furnace (Fig. 6) [37]. In the case of (101) crystal plane for the rta-CuTN and the tf-CuTN crystallite size is equal to 8.6 nm and 9.5 nm, respectively. Crystallite size of (112) crystal plane for rta-CuTN and the tf-CuTN reaches 15.5 nm and 34.1 nm, respectively. Furthermore, decrease in intensity can be correlated with the presence of oxygen vacancies [38].

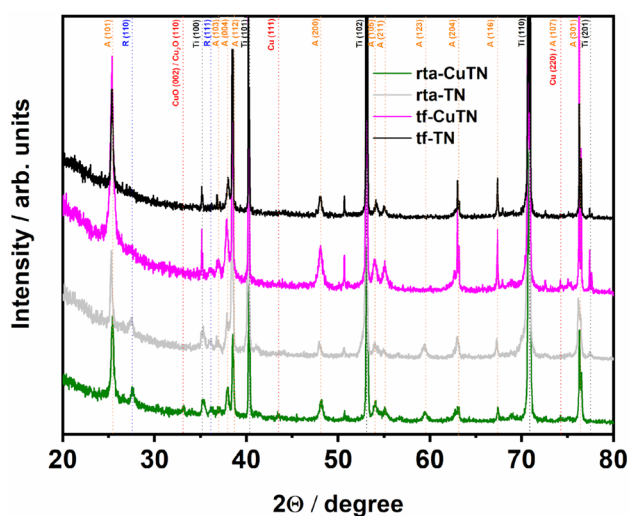


Figure 6 XRD patterns of pure TN and TN with developed area and modified by copper.

Characterization of surface chemistry

The chemical nature of copper species on titania, depending on thermal treatment, was studied using XPS. Most notably, the $\text{Cu}2p$ spectra recorded after RTA in hydrogen and TF in air atmosphere are shown in Fig. 7a, b, respectively. These deconvoluted spectra reveal surface complexity of the samples with a multitude of signals originating from numerous Cu chemical states. The primary $\text{Cu}2p_{3/2}$ peak was recognized at 932.7 eV and may originate from Cu^0 or Cu^+ oxidation states [39]. These can be possibly distinguished based on the Cu_{KLL} Auger spectra, shown in Fig. 7c. Here, a very strong peak at 916.5 eV confirms the presence of Cu^+ for both treatments. In the case of the rta-CuTN electrode, the weak peak located at 919 eV can be attributed to metallic copper [40]. However, it should

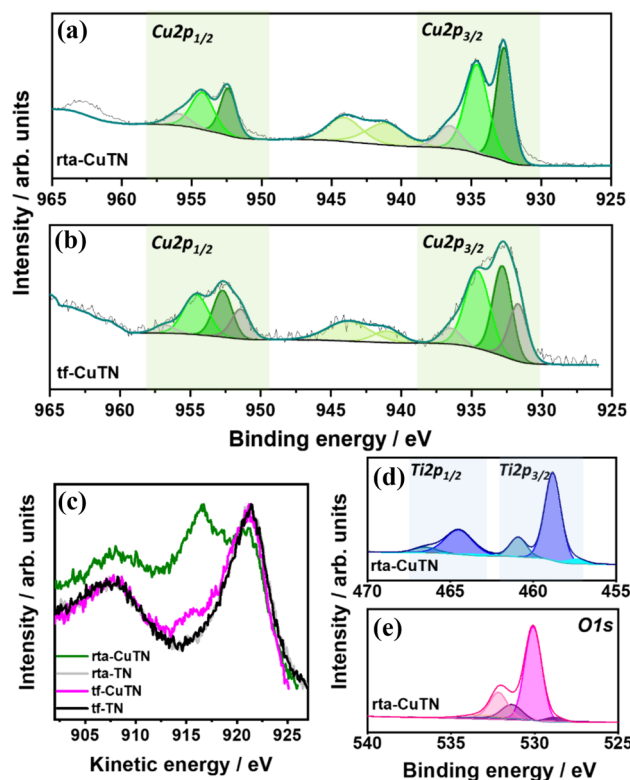


Figure 7 High-resolution XPS CuTN spectra after **a** RTA and **b** TF treatments; **c** Cu_{KLL} Auger spectra with TN as a reference. rta-CuTN **(d)** $\text{Ti}2p$ and **e** $\text{O}1s$ spectra.

be taken into account that peaks related to oxides and metallic copper on the Auger spectra are close to each other [40].

Two other components visible at $\text{Cu}2p$ spectra and shifted at +1.8 and +3.7 eV from 932.7 eV originate from various Cu^{2+} species, most likely in the form of oxides and carbonate dihydroxyoxides [41], the latter of which is a consequence of sample exposure to atmospheric air. The Cu^{2+} presence is easily distinguishable by strong satellite features in the 940–945 eV range. Notably, regardless the thermal treatment procedure, the Cu^+ to Cu^{2+} ratio remains on a nearly constant level of 0.7:1 for RTA and 0.6:1 for TF, respectively, possibly indicating that there are no significant changes in the surface film. However, in the case of the tf-CuTN, a fourth notable component was observed at 932.1 eV. The origin of this signal is not clear; however, such a position of the binding energy could be possible in case of structural reconfiguration and formation of CuTi intermetallic bonds.

Finally, the $\text{Ti}2p$ (Fig. 7d) and $\text{O}1s$ (Fig. 7e) spectra confirm the typical chemical nature of titania

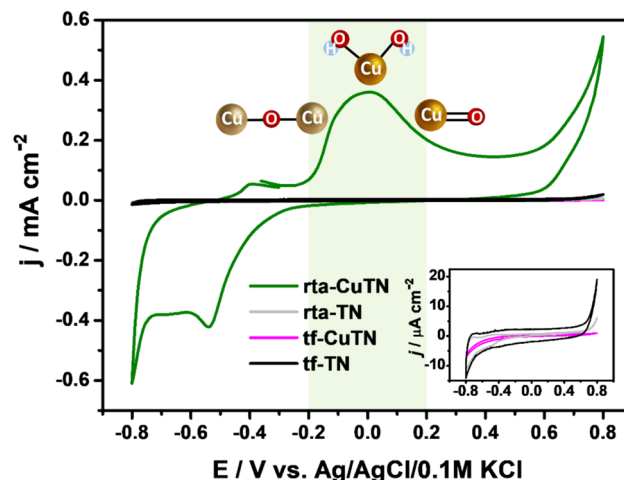


Figure 8 Cyclic voltammograms for pure TN and TN with increased area modified by copper registered in 0.1 M NaOH (the drawings in the curve describe the formation of Cu_2O , $\text{Cu}(\text{OH})_2$ and CuO species by Cu oxidation in particular potential range). Inset: the magnification of the CV curves recorded for rta-TN, tf-CuTN and tf-TN.

nanotubes, with TiO_2 -specific $\text{Ti}2p_{3/2}$ at 458.8 eV and $\text{O}1s$ at 530.1 eV, likewise previously reported by our group [42]. The $\text{Ti}2p$ peak located at 457.3 eV can be assigned to Ti^{3+} [43]. In the case of $\text{O}1s$ peak at 531.2 eV can be described as Ti_2O_3 oxide, non-lattice oxygen and oxygen vacancies [44, 45]. Furthermore, the peak located at 532.2 eV also can be attributed to non-lattice oxygen and a surface adsorbed OH group [46]. Lower peak values at 528.7 eV may be associated with nonbridging oxygen [46, 47].

Electrochemical and photoelectrochemical properties of obtained electrodes

The cyclic voltammetry measurements were taken for pure TN and TN with increased surface area modified by copper in order to characterize electrochemical activity (Fig. 8). Measurements were taken in 0.1 M NaOH solution in the range of -0.8 V to $+0.8$ V versus $\text{Ag}/\text{AgCl}/0.1$ M KCl. The alkaline solution was chosen because copper oxides exhibit the best stability in such environment [48]. The significant increase of capacitive current as well as strong faradaic peaks is observed for rta-CuTN with increased area modified by copper rapidly thermal hydrogenated. For the rta-CuTN electrode, oxidation of Cu to Cu_2O and CuO occurs from -0.2 V to $+0.2$ V versus $\text{Ag}/\text{AgCl}/0.1$ M KCl during the anodic polarization

[42, 49]. XRD and XPS analysis already indicated the presence of Cu^0 and Cu^+ oxidation states for the rta-CuTN electrode. The current density at 0 V versus Ag/AgCl/0.1 M KCl is equal to $360 \mu\text{A}/\text{cm}^2$ for the rta-CuTN and is three orders of magnitude higher than for the tf-CuTN. The material was stable during CV, and cycles overlap. The performance of various CuO nanostructures as a supercapacitor was shown by Luo et al. [50] in 1 M KOH electrolyte. In the case of those structures, redox peaks originating from the faradic reaction of Cu^+ and Cu^{2+} to Cu_2O and CuO can be seen. Moreover, the presence of Cu^{2+} is associated with OH^- ions which oxidize copper to $\text{Cu}(\text{OH})_2$ [51]. Such pseudocapacitive character for CuPt nanoparticles deposited on a carbon electrode was also shown by Sachin et al. [52] The current density for CuPt nanoparticles at -0.1 V versus Hg/HgO measured in 0.5 M KOH was equal to ca. $2 \text{ mA}/\text{cm}^2$. A similar result was obtained in our work for the rta-CuTN electrode at ca. 0 V versus Ag/AgCl/0.1 M KCl in 0.1 M KHCO_3 and K_2CO_3 electrolyte with addition of 0.5 M NaOH (Fig. 11b). The observed activity can indicate that the increase of current density from $0.4 \text{ mA}/\text{cm}^2$ to $1.2 \text{ mA}/\text{cm}^2$ (see Fig. 11b) due to higher OH^- concentration is caused by two

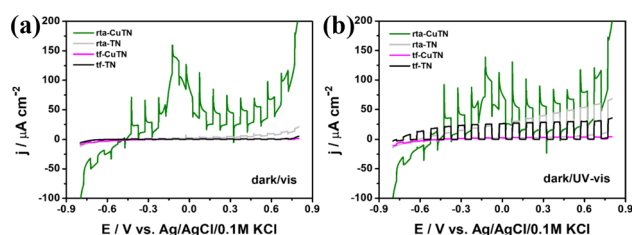


Figure 9 Linear voltammetry curves for pure TN and TN with an increased area modified by copper measured in 0.1 M NaOH under (a) visible and (b) UV-vis light illumination.

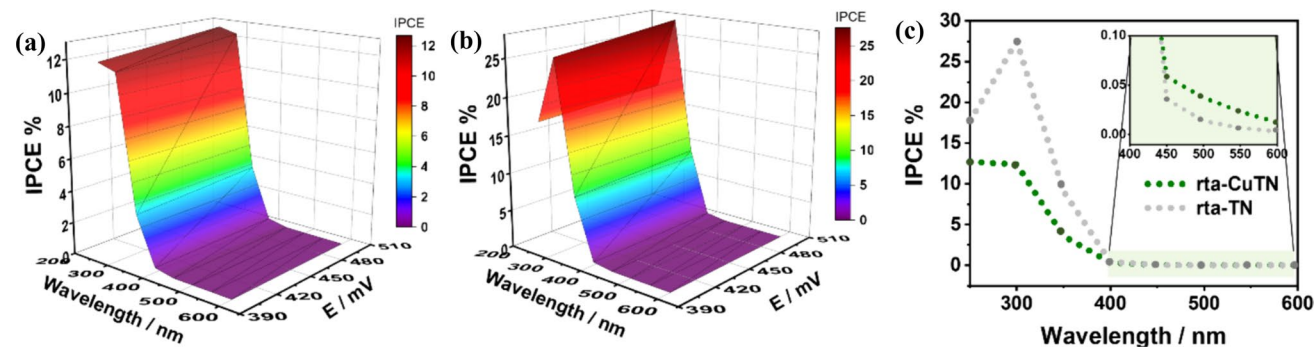


Figure 10 IPCE of (a) rta-CuTN and (b) rta-TN, (c) the comparison of IPCE values for different wavelengths registered at +0.5 V.

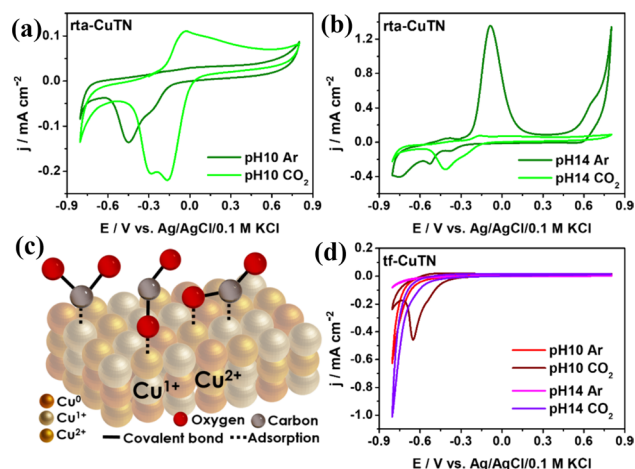


Fig. 11 CVs curves for (a, b) rta-CuTN electrode, (c) schematic representation of adsorbed CO_2 on copper oxides (carbon, oxygen and carbon-oxygen bonds), (d) CVs curves for the tf-CuTN electrode registered in 0.1 M KHCO_3 and K_2CO_3 without or with NaOH. The measurements were taken in the electrolyte deaerated with argon or saturated with CO_2

reactions occurring at similar potentials, namely oxidation of Cu to Cu_2O and CuO as well as formation of $\text{Cu}(\text{OH})_2$. Figure 8 shows the reduction peak recorded at -0.5 V versus Ag/AgCl/0.1 M KCl for the rta-CuTN electrode equals to ca. $-420 \mu\text{A}/\text{cm}^2$ and can be attributed to the reduction of Cu_2O to Cu [31].

In order to characterize the photoelectrochemical activity of the electrodes, linear voltammetry measurements were taken in 0.1 M NaOH solution in the range from -0.8 V to $+0.8$ V versus Ag/AgCl/0.1 M KCl under vis and UV-vis light illumination (Fig. 9). The strongest enhancement of photocurrent under visible light is obtained for the rta-CuTN sample. The photocurrent recorded at $+0.5$ V is equal to $28 \mu\text{A}/\text{cm}^2$ which is 14 times higher than for the rta-TN electrode and

35 times higher than for the tf-CuTN (Fig. 9a). In the case of the photocurrent registered under UV–vis illumination values for rta-CuTN, rta-TN, tf-CuTN, and tf-TN are equal to $52 \mu\text{A}/\text{cm}^2$, $45 \mu\text{A}/\text{cm}^2$, $3 \mu\text{A}/\text{cm}^2$, and $29 \mu\text{A}/\text{cm}^2$, respectively. The best photoactivity of the rta-CuTN under visible as well as UV–vis light is in accordance with the absorbance band in Fig. 4a. According to Cui et al. [53] hydrogenated TiO_2 is characterized by enhanced adsorption of carbon species as well as formation of defects and oxygen vacancies which can improve photocatalytic activity. In the case of the rta-CuTN electrode, the presence of oxygen vacancies was confirmed by XPS and XRD measurements. It should be highlighted that for hydrogenated copper-modified TiO_2 nanotubes positive photocurrent spikes, which correspond to the accumulation of holes in the electrode space charge layer during illumination [54] can be observed in the range from -0.6 V to $+0.8 \text{ V}$. The generation of photocurrent is a complex phenomenon. According to Liqiang et al. [55] photoactivity of TiO_2 depends on the number of generated carriers; however, the efficiency depends on recombination, transfer, and capture processes. To deeply understand photoelectrochemical activity, IPCE measurements for the best electrodes were taken (Fig. 10).

Figure 10 shows IPCE curves registered for the rta-TN and rta-CuTN electrodes. It should be underlined that the significant enhancement of photocurrent under vis and UV–vis light registered during linear voltammetry measurements for the rta-CuTN electrode is related to the presence of Cu_2O and CuO . Linear voltammetry measurements allow distinguishing between two types of light interaction with copper oxides such as electron–hole charge separation and photogenerated charge accumulation [31]. Such phenomena can occur during linearly changing potentials, which allows the simultaneous formation of new copper oxides that accumulate the photogenerated charge. These charges can be further transported towards the TiO_2 platform. However, in the case of IPCE, measurements are taken at the selected potential, for various wavelengths sweeping from the shortest to the longest in the given range. In this case, it is hard to effectively accumulate the charge. Such a phenomenon is caused by the difference in how the potential is applied to the electrode with a given scan rate, for example, 10 mV/s or 50 mV/s . During linear voltammetry measurements no relaxation process of accumulated charge occurs. This phenomenon is not observed for IPCE measurements where the measurement dynamics are similar

to the chronoamperometry technique. More dominant are electron–hole charge separation processes which are typical for TiO_2 structures. Therefore, the highest IPCE is obtained for UV light where TiO_2 photoactivity takes place. The IPCE for the rta-TN for 300 nm is equal to ca. 25% (Fig. 10c).

Figure 11 shows the CV curves for the rta-CuTN and the tf-CuTN electrodes in the Ar-saturated and CO_2 -saturated 0.1 M KHCO_3 and K_2CO_3 electrolyte without or with addition of NaOH . According to Wang et al. [56] CO_2 can bind to the surface of CuO at negative potentials, on the potential where CuO is not yet reduced to Cu^{1+} or Cu^0 . This is a process of CO_2 adsorption on the surface of the material. The surface is covered by CO_2 molecules and because of that, the reduction of copper can be inhibited by carbon dioxide. The schematic representation of CO_2 adsorbed on the surface is presented in Fig. 11c [57, 58]. Carbon dioxide molecule interacts with a single-metal atom via carbon, oxygen, or mixed carbon–oxygen bond. It should be mentioned that CO_2 adsorption can be divided into physisorption and chemisorption [59]. Therefore, the higher reduction currents registered from -0.1 to -0.4 V versus $\text{Ag}/\text{AgCl}/0.1 \text{ M KCl}$ (Fig. 11a,b) are related to CO_2 adsorption after electrolyte saturation. The rta-CuTN electrode has intense reduction peak with current density of $-220 \mu\text{A}/\text{cm}^2$ and $-320 \mu\text{A}/\text{cm}^2$ after CO_2 saturation for $\text{pH} = 10$ and $\text{pH} = 14$, respectively. Furthermore, the reduction peak for hydrogenated samples is shifted towards more positive values after CO_2 addition. According to Zhou et al. [60] annealing in reducing atmosphere can create defects such as oxygen vacancy, which improve adsorption of the molecules on the surface.

In the case of TN with increased area modified by copper annealed in conventional tube furnace, the enhanced current density at -0.8 V versus $\text{Ag}/\text{AgCl}/0.1 \text{ M KCl}$ for 10 and 14 pH solutions after CO_2 saturation indicates the electrocatalytic ability towards CO_2 reduction reaction (Fig. 11d) [61]. It can be clearly seen that increasing the pH from 10 to 14 resulted in a higher current density with an increase from $200 \mu\text{A}/\text{cm}^2$ to $1 \text{ mA}/\text{cm}^2$ at -0.8 V . Therefore, it can be assumed that CO_2 reduction on the tf-CuTN electrode improves with increasing solution alkalinity. According to Nitopi et al. [61] the pH has significant impact on reaction products, selectivity, and efficiency of the carbon dioxide reduction reaction. Furthermore, basic electrolytes can lead to improvement in production of

multicarbon compounds as well as higher selectivity [62]. It should be also noted that the reduction peak registered at -0.6 V versus Ag/AgCl/0.1 M KCl in CO_2 saturated 0.1 M KHCO_3 and K_2CO_3 electrolyte at pH 10 can be not only attributed to transition products of carbon dioxide reduction reaction but also to bicarbonates reduction products which are dissolved in the solution [63].

Conclusions

In here, we presented a fabrication route of ordered spaced TiO_2 nanotubes, treated with TiCl_4 solution, and coated by a 10 nm copper layer. Modified electrodes were thermally treated via rapid annealing in a hydrogen atmosphere and in air in conventional furnace with slow, gradual heating. In order to increase the surface area, the titania nanotubes were modified with the use of TiCl_4 that provides higher roughness to initially smooth nanotubes, as was shown by SEM investigations. Cu sputtering and thermal processing lead to the final version of the electrode material. The photoluminescence measurements indicated the lowest emission in visible light range especially for blue light for the rta-CuTN electrode which may be correlated with the shallow level of oxygen vacancy with one trapped electron. For the hydrogenated TN modified by copper Cu (111), Cu (220), Cu_2O (110) and CuO (002) crystallographic planes were recognized. The presence of Cu^0 , Cu^{1+} and Cu^{2+} copper states was confirmed by X-ray photoelectron spectroscopy. Furthermore, the best photoelectrochemical activity was obtained for the rta-CuTN electrode. The current density increased 35 and 17 times under UV-vis and visible light illumination, respectively, for rapid thermal hydrogenated copper oxides in comparison to conventionally annealed TiO_2 nanotubes with increased area modified by copper. Moreover, the obtained results indicate the possibility of tuning the efficiency of CO_2 adsorption or the CO_2 reduction reaction on copper oxides by changing the annealing procedure. Rapid thermal annealing in hydrogen favours CO_2 adsorption. Carbon dioxide is physically or chemically adsorbed on Cu^{1+} and Cu^{2+} where defects such as oxygen vacancy improve its adsorption. Using the strategies reported here will thus enable improved photoelectrodes in the future.

Acknowledgement

People who contributed to the work in the manuscript but who are not named in the author list: not applicable. This work is financially supported by the National Science Centre (Poland): Grant no. 2020/39/I/ST5/01781. RWC and VM acknowledge support from the Deutsche Forschungsgemeinschaft (DFG)–Project number 465220299.

Author contribution

Not applicable.

Funding

Narodowe Centrum Nauki, 2020/39/I/ST5/01781, Katarzyna Siuzdak, Deutsche Forschungsgemeinschaft, 465220299, Ryan Crisp.

Data and code availability

DOI to an electronic repository.

Declarations

Conflicts of interest The authors declare no competing financial interest.

Ethical approval Not applicable.

Supplementary Information The online version contains supplementary material available at <https://doi.org/10.1007/s10853-024-10223-4>.

Open Access This article is licensed under a Creative Commons Attribution 4.0 International License, which permits use, sharing, adaptation, distribution and reproduction in any medium or format, as long as you give appropriate credit to the original author(s) and the source, provide a link to the Creative Commons licence, and indicate if changes were made. The images or other third party material in this article are included in the article's Creative Commons licence, unless indicated otherwise in a credit line to the material. If material is not included in the article's

Creative Commons licence and your intended use is not permitted by statutory regulation or exceeds the permitted use, you will need to obtain permission directly from the copyright holder. To view a copy of this licence, visit <http://creativecommons.org/licenses/by/4.0/>.

References

- [1] Wotzka A, Dühren R, Suhrbier T, Polyakov M, Wohlrab S (2020) Adsorptive capture of CO₂ from air and subsequent direct esterification under mild conditions. *ACS Sustain Chem Eng* 8:5013–5017. <https://doi.org/10.1021/acssuschemeng.0c00247>
- [2] Olajire AA (2010) CO₂ capture and separation technologies for end-of-pipe applications—a review. *Energy* 35:2610–2628. <https://doi.org/10.1016/j.energy.2010.02.030>
- [3] Inoue T, Fujishima A, Konishi S, Honda K (1979) Photoelectrocatalytic reduction of carbon dioxide in aqueous suspensions of semiconductor powders. *Nature* 277:637–638. <https://doi.org/10.1038/277637a0>
- [4] de Almeida J, Pacheco MS, de Brito JF, de Arruda RC (2020) Contribution of Cu_xO distribution, shape and ratio on TiO₂ nanotubes to improve methanol production from CO₂ photoelectroreduction. *J Solid State Electrochem* 24:3013–3028. <https://doi.org/10.1007/s10008-020-04739-3>
- [5] Wu N, Wang J, Tafen DN, Wang H, Zheng JG, Lewis JP, Manivannan A (2010) Shape-enhanced photocatalytic activity of single-crystalline anatase TiO₂(101) nanobelts. *J Am Chem Soc* 132:6679–6685. <https://doi.org/10.1021/ja909456f>
- [6] Song F, Zhao Y, Zhong Q (2013) Adsorption of carbon dioxide on amine-modified TiO₂ nanotubes. *J Environ Sci* 25:554–560. [https://doi.org/10.1016/s1001-0742\(12\)60097-7](https://doi.org/10.1016/s1001-0742(12)60097-7)
- [7] Jen HP, Lin MH, Li LL, Wu HP, Huang WK, Cheng PJ, Diao EWG (2013) High-performance large-scale flexible dye-sensitized solar cells based on anodic TiO₂ nanotube arrays. *ACS Appl Mater Interfaces* 5:10098–10104. <https://doi.org/10.1021/am402687j>
- [8] Yuan X, Zheng M, Ma L, Shen W (2010) High-speed growth of TiO₂ nanotube arrays with gradient pore diameter and ultrathin tube wall under high-field anodization. *Nanotechnology* 21:405302–405312. <https://doi.org/10.1088/0957-4484/21/40/405302>
- [9] Lipińska W, Grochowska K, Karczewski J, Coy E, Siuzdak K (2022) Electrocatalytic oxidation of methanol, ethylene glycol and glycerine in alkaline media on TiO₂ nanotubes decorated with AuCu nanoparticles for an application in fuel cells. *J Mater Sci* 57:13345–13361. <https://doi.org/10.1007/s10853-022-07471-7>
- [10] Lipińska W, Grochowska K, Karczewski J, Ryl J, Cenian A, Siuzdak K (2020) Thermally tuneable optical and electrochemical properties of Au-Cu nanomosaic formed over the host titanium dimples. *Chem Eng J* 399:125673. <https://doi.org/10.1016/j.cej.2020.125673>
- [11] Hannula M, Ali-Löytty H, Lahtonen K, Sarlin E, Saari J, Valden M (2018) Improved stability of atomic layer deposited amorphous TiO₂ photoelectrode coatings by thermally induced oxygen defects. *Chem Mater* 30:1199–1208. <https://doi.org/10.1021/acs.chemmater.7b02938>
- [12] Zhang K, Park JH (2016) Surface localization of defects in black TiO₂: enhancing photoactivity or reactivity. *J Phys Chem Lett* 8:199–207. <https://doi.org/10.1021/acs.jpcclett.6b02289>
- [13] Huo J, Hu Y, Jiang H, Li C (2014) In situ surface hydrogenation synthesis of Ti³⁺ self-doped TiO₂ with enhanced visible light photoactivity. *Nanoscale* 6:9078–9084. <https://doi.org/10.1039/c4nr00972j>
- [14] Li S, Qiu J, Ling M, Peng F, Wood B, Zhang S (2013) Photoelectrochemical characterization of hydrogenated TiO₂ nanotubes as photoanodes for sensing applications. *ACS Appl Mater Interfaces* 5:11129–11135. <https://doi.org/10.1021/am403325a>
- [15] Wu MC, Huang WK, Lin TH, Lu YJ (2018) Photocatalytic hydrogen production and photodegradation of organic dyes of hydrogenated TiO₂ nanofibers decorated metal nanoparticles. *Appl Surf Sci* 469:34–43. <https://doi.org/10.1016/j.apsusc.2018.10.240>
- [16] Huang S, Zhang Q, Huang X, Guo X, Deng M, Li D, Meng Q (2010) Fibrous CdS/CdSe quantum dot co-sensitized solar cells based on ordered TiO₂ nanotube arrays. *Nanotechnology* 21:375201. <https://doi.org/10.1088/0957-4484/21/37/375201>
- [17] Meen TH, Jhuo YT, Chao SM, Lin NY, Ji LW, Tsai JK, Huang CJ (2012) Effect of TiO₂ nanotubes with TiCl₄ treatment on the photoelectrode of dye-sensitized solar cells. *Nanoscale Res Lett* 7:579. <https://doi.org/10.1186/1556-276X-7-579>
- [18] Reyes-Coronado D, Rodríguez-Gattorno G, Espinosa-Pesqueira ME, Cab C, de Coss R, Oskam G (2008) Phase-pure TiO₂ nanoparticles: anatase, brookite and rutile. *Nanotechnology* 19:145605. <https://doi.org/10.1088/0957-4484/19/14/145605>
- [19] Molenda Z, Grochowska K, Karczewski J, Ryl J, Darowicki K, Rysz J, Cenian A, Siuzdak K (2020) The influence of the Cu₂O deposition method on the structure, morphology and

- photoresponse of the ordered TiO₂ NTs/Cu₂O heterojunction. *Mater Res Express* 6:1250b6. <https://doi.org/10.1088/2053-1591/ab6195>
- [20] Gharaei SK, Abbasnejad M, Maezono R (2018) Band-gap reduction of photocatalytic TiO₂ nanotube by Cu doping. *Sci Rep* 8:14192. <https://doi.org/10.1038/s41598-018-32130-w>
- [21] Lee JS, Kim KH, Kim CS, Choi HW (2015) Achieving enhanced dye-sensitized solar cell performance by TiCl₄/Al₂O₃ doped TiO₂ nanotube array photoelectrodes. *J Nanomater* 4:1. <https://doi.org/10.1155/2015/545818>
- [22] Siuzdak K, Szkoda M, Lisowska-Oleksiak A, Karczewski J, Ryl J (2016) Highly stable organic–inorganic junction composed of hydrogenated titania nanotubes infiltrated by a conducting polymer. *RSC Adv* 6:33101–33110. <https://doi.org/10.1039/C6RA01986B>
- [23] Lei Y, Zhang LD, Meng GW, Li GH, Zhang XY, Liang CH, Wang SX (2001) Preparation and photoluminescence of highly ordered TiO₂ nanowire arrays. *Appl Phys Lett* 78:1125–1127. <https://doi.org/10.1063/1.1350959>
- [24] Choudhury B, Choudhury A (2013) Tailoring luminescence properties of TiO₂ nanoparticles by Mn doping. *J Lumin* 136:339–346. <https://doi.org/10.1016/j.jlumin.2012.12.011>
- [25] Choudhury B, Dey M, Choudhury A (2013) Shallow and deep trap emission and luminescence quenching of TiO₂ nanoparticles on Cu doping. *Appl Nanosci* 4:499–506. <https://doi.org/10.1007/s13204-013-0226-9>
- [26] Choudhury B, Choudhury A, Borah D (2015) Interplay of dopants and defects in making Cu doped TiO₂ nanoparticle a ferromagnetic semiconductor. *J Alloy Compd* 646:692–698. <https://doi.org/10.1016/j.jallcom.2015.06.199>
- [27] Wu WY, Chang YM, Ting JM (2010) Room-temperature synthesis of single-crystalline anatase TiO₂ nanowires. *Cryst Growth Des* 10:1646–1651. <https://doi.org/10.1021/am1005892>
- [28] Palliyaguru L, Kulathunga US, Jayarathna LI, Jayaweera CD, Jayaweera PM (2020) A simple and novel synthetic route to prepare anatase TiO₂ nanopowders from natural ilmenite via the H₃PO₄/NH₃ process. *Int J Miner Metall Mater* 27:846–855. <https://doi.org/10.1007/s12613-020-2030-3>
- [29] Peng X, Wang Z, Huang P, Chen X, Fu X, Dai W (2016) Comparative study of two different TiO₂ film sensors on response to H₂ under UV light and room temperature. *Sensors* 16:1249. <https://doi.org/10.3390/s16081249>
- [30] Sakar A, Khan GG (2019) The formation and detection techniques of oxygen vacancies in titanium oxide-based nanostructures. *Nanoscale* 11:3414–3444. <https://doi.org/10.1039/C8NR09666J>
- [31] Lipińska W, Grochowska K, Karczewski J, Ryl J, Siuzdak K (2022) Temperature-controlled nanomosaics of AuCu bimetallic structure towards smart light management. *J Mater Sci: Mater Electron* 33:19385. <https://doi.org/10.1007/s10854-022-08775-9>
- [32] El-Desoky MM, Morad I, Wasfy MH, Mansour AF (2020) Synthesis, structural and electrical properties of PVA/TiO₂ nanocomposite films with different TiO₂ phases prepared by sol-gel technique. *J Mater Sci: Mater Electron* 31:17574. <https://doi.org/10.1007/s10854-020-04313-7>
- [33] Betancourt-Galindo R, Reyes-Rodríguez PY, Puente-Urbina BA, Avila-Orta CA, Rodríguez-Fernández OS, Cadenas-Pliego G, García-Cerda LA (2014) Synthesis of copper nanoparticles by thermal decomposition and their antimicrobial properties. *J Nanomater* 1:5. <https://doi.org/10.1155/2014/980545>
- [34] Tamuly C, Saikia I, Hazarika M, Das MR (2014) Reduction of aromatic nitro compounds catalyzed by biogenic CuO nanoparticles. *RSC Adv* 4:53229–53236. <https://doi.org/10.1039/C4RA10397A>
- [35] Sajeev A, Paul AM, Nivetha R, Gothandapani K, Gopal TS, Jacob G, Muthuramamoorthy M, Pandiaraj S, Alodhayb A, Kim SY, Le QV, Show PL, Jeong SK, Grace AN (2022) Development of Cu₃N electrocatalyst for hydrogen evolution reaction in alkaline medium. *Sci Rep* 12:2004. <https://doi.org/10.1038/s41598-022-05953-x>
- [36] Wu M, Zhang Z, Xu X, Zhang Z, Duan Y, Dong J, Liu K (2020) Seeded growth of large single-crystal copper foils with high-index facets. *Nature* 581:406–410. <https://doi.org/10.1038/s41586-020-2298-5>
- [37] Bakri AS, Sahdan MZ, Adriyanto F, Raship NA, Said NDM, Abdullah SA, Rahim MS (2016) Effect of annealing temperature of titanium dioxide thin films on structural and electrical properties. *Int Conf Eng Sci Nanotechnol AIP Publ.* 1788:030030. <https://doi.org/10.1063/1.4968283>
- [38] Lu R, Wang C, Wang X, Wang Y, Wang N, Chou J, Chen S (2018) Effects of hydrogenated TiO₂ nanotube arrays on protein adsorption and compatibility with osteoblast-like cells. *Int J Nanomed* 13:2037–2049. https://doi.org/10.1111/clr.57_13358
- [39] Jiang P, Prendergast D, Borondics F, Porsgaard S, Giovanetti L, Pach E, Salmeron M (2013) Experimental and theoretical investigation of the electronic structure of Cu₂O and CuO thin films on Cu(110) using x-ray photoelectron and absorption spectroscopy. *J Chem Phys* 138:024704. <https://doi.org/10.1063/1.4773583>
- [40] Popok VN, Novikov SM, Lebedinskij YY, Markeev AM, Andreev AA, Trunkin IN, Volkov VS (2021) Gas-aggregated copper nanoparticles with long-term Plasmon

- resonance stability. *Plasmonics* 16:333–340. <https://doi.org/10.1007/s11468-020-01287-4>
- [41] Park H, Kim SE (2019) Two-step plasma treatment on copper surface for low temperature Cu thermo-compression bonding. *IEEE Trans Compon Packag Manuf Technol* 10:332–338. <https://doi.org/10.1109/TCPMT.2019.2928323>
- [42] Lipinska W, Grochowska K, Ryl J, Karczewski J, Siuzdak K (2021) Influence of annealing atmospheres on photoelectrochemical activity of TiO₂ nanotubes modified with AuCu nanoparticles. *ACS Appl Mater Interfaces* 13:52967–52977. <https://doi.org/10.1021/acsmi.1c16271>
- [43] Shvab R, Hryha E, Nyborg L (2016) Surface chemistry of the titanium powder studied by XPS using internal standard reference. *Powder Metall* 60:42–48. <https://doi.org/10.1080/00325899.2016.1271092>
- [44] Bharti B, Kumar S, Lee HN, Kumar R (2016) Formation of oxygen vacancies and Ti³⁺ state in TiO₂ thin film and enhanced optical properties by air plasma treatment. *Sci Rep* 6:32355. <https://doi.org/10.1038/srep32355>
- [45] Majumder S, Choudhary RJ, Tripathi M, Phase DM (2018) Effect of calcination routes on phase formation of BaTiO₃ and their electronic and magnetic properties. *AIP Conf Proc* 1953:110020–110021. <https://doi.org/10.1063/1.5033045>
- [46] Zhang S, Zhang X, Peng H, Wen L, Qiu G, Hu M, Bai C (2014) Structure analysis of CaO–SiO₂–Al₂O₃–TiO₂ slag by molecular dynamics simulation and FT-IR spectroscopy. *ISIJ Int* 54:734–742. <https://doi.org/10.2355/isijinternational.54.734>
- [47] Hsu JC, Wang PW, Lee CC (2006) X-ray photoelectron spectroscopy study of thin TiO₂ films cosputtered with Al. *Appl Opt* 45:4303. <https://doi.org/10.1364/AO.45.004303>
- [48] Gomez Becerra J, Salvarezza RC, Arvia AJ (1988) The influence of slow Cu(OH)₂ phase formation on the electrochemical behaviour of copper in alkaline solutions. *Electrochim Acta* 33:613–621. [https://doi.org/10.1016/0013-4686\(88\)80059-8](https://doi.org/10.1016/0013-4686(88)80059-8)
- [49] Bogdanowicz R, Ryl J, Darowicki K, Kosmowski BB (2008) Ellipsometric study of oxide formation on Cu electrode in 0.1 M NaOH. *J Solid State Electrochem* 13:1639–1644. <https://doi.org/10.1007/s10008-008-0650-z>
- [50] Lu Y, Yan H, Qiu K, Cheng J, Wang W, Liu X, Tang Ch, Kim JK, Luo Y (2015) Hierarchical porous CuO nanostructures with tunable properties for high performance supercapacitors. *RSC Adv* 5:10773–10781. <https://doi.org/10.1039/C4RA16924G>
- [51] Wang G, Huang J, Chen S, Gao Y, Cao D (2011) Preparation and supercapacitance of CuO nanosheet arrays grown on nickel foam. *J Power Sources* 196:5756–5760. <https://doi.org/10.1016/j.jpowsour.2011.02.049>
- [52] Sachin DG, Sarkar A (2016) Electrochemical study of bulk and monolayer copper in alkaline solution. *J Electrochem Soc* 163:H252–H259. <https://doi.org/10.1149/2.0071605jes>
- [53] Cui Z, Zhao M, Que X, Wang J, Xu Y, Ghazzal MN, Colbeau-Justin Ch, Pan D, Wu W (2021) Facile vacuum annealing-induced modification of TiO₂ with an enhanced photocatalytic performance. *ACS Omega* 6:27121–27128. <https://doi.org/10.1021/acsomega.1c03762>
- [54] Tamirat AG, Dubale AA, Su WN, Chen HM, Hwang BJ (2017) Sequentially surface modified hematite enables lower applied bias photoelectrochemical water splitting. *Phys Chem Chem Phys* 19:20881–20890. <https://doi.org/10.1039/C7CP02890C>
- [55] Liqiang J, Yichun Q, Baiqi W, Shudan L, Baojiang J, Libin Y, Jiazhong S (2006) Review of photoluminescence performance of nano-sized semiconductor materials and its relationships with photocatalytic activity. *Sol Energy Mater Sol Cells* 90:1773–1787. <https://doi.org/10.1016/j.solmat.2005.11.007>
- [56] Wang L, Gupta K, Goodall JBM, Darr JA, Holt KB (2017) In situ spectroscopic monitoring of CO₂ reduction at copper oxide electrode. *Faraday Discuss* 197:517–532. <https://doi.org/10.1039/C6FD00183A>
- [57] Xiao C, Zhang J (2012) Architectural design for enhanced C₂ product selectivity in electrochemical CO₂ reduction using Cu-based catalysts: a review. *ACS Nano* 15:7975. <https://doi.org/10.1021/acsnano.0c10697>
- [58] Freund HJ, Roberts MW (1996) Surface chemistry of carbon dioxide. *Surf Sci Rep* 25:225–273. [https://doi.org/10.1016/s0167-5729\(96\)00007-6](https://doi.org/10.1016/s0167-5729(96)00007-6)
- [59] Burghaus U (2014) Surface chemistry of CO₂—Adsorption of carbon dioxide on clean surfaces at ultrahigh vacuum. *Prog Surf Sci* 89:161–217. <https://doi.org/10.1016/j.progsurf.2014.03.00>
- [60] Zhou Y, Liu Y, Liu P, Zhang W, Xing M, Zhang JA (2015) Facile approach to further improve the substitution of nitrogen into reduced TiO_{2-x} with an enhanced photocatalytic activity. *Appl Catal B* 170:66–73. <https://doi.org/10.1016/j.apcatb.2015.01.036>
- [61] Sheelam A, Muneeb A, Talukdar B, Ravindranath R, Huang SJ, Kuo CH, Sankar R (2020) Flexible and free-standing polyvinyl alcohol-reduced graphene oxide-Cu₂O/CuO thin films for electrochemical reduction of carbon dioxide. *J Appl Electrochem* 50:979–991. <https://doi.org/10.1007/s10800-020-01450-z>
- [62] Nitopi S, Bertheussen E, Scott SB, Liu X, Engstfeld AK, Horch S, Stephens IEL, Chan K, Hahn Ch, Nørskov JK, Jaramillo TFI (2019) Progress and perspectives of electrochemical CO₂ reduction on copper in aqueous electrolyte.

Chem Rev 119:7610–7672. <https://doi.org/10.1021/acs.chemrev.8b00705>

- [63] Tapan NA (2016) CO₂ electroreduction on P4VP modified copper deposited gas diffusion layer electrode: pH effect. Mater Renew Sustain Energy 5:19-29. <https://doi.org/10.1007/s40243-016-0082-0>

Publisher's Note Springer Nature remains neutral with regard to jurisdictional claims in published maps and institutional affiliations.